Journal of the Taiwan Institute of Chemical Engineers 114 (2020) 91–102

Contents lists available at ScienceDirect

Journal of the Taiwan Institute of Chemical Engineers

journal homepage: www.elsevier.com/locate/jtice

Green synthesis of H-ZSM-5 zeolite-anchored O-doped g−C_3N_4 for photodegradation of Reactive Red 195 (RR 195) under solar light

Xuan Nui Pham[a,*], Hoa Thi Nguyen[a], Tuyet Nhung Pham[a,b], T.-Thanh-Bao Nguyen[c], Manh B. Nguyen[d], Van Thi-T. Tran[e], Huan V. Doan[a,f]

[a] Department of Chemical Engineering, Hanoi University of Mining and Geology, 18 Pho Vien, Duc Thang, Bac Tu Liem District, Hanoi, Vietnam
[b] Phenikaa University Nano Institute (PHENA), PHENIKAA University, Hanoi 12116, Vietnam
[c] Institute of Physics, Vietnam Academy of Science and Technology, 18C Hoang Quoc Viet, Hanoi, Vietnam
[d] Institute of Research and Development, Duy Tan University, Da Nang 550000, Vietnam
[e] Department of Chemistry, Hue Science College, Hue University, 77 Nguyen Hue Str., Hue City, Vietnam
[f] School of Chemistry, University of Bristol, Bristol BS8 1TS, UK

ARTICLE INFO

Article History:
Received 13 July 2020
Revised 22 August 2020
Accepted 6 September 2020
Available online 29 September 2020

Keywords:
O−g−C_3N_4/H-ZSM-5
O−g−C_3N_4
Zeolite
Photodegradation
RR 195

ABSTRACT

A novel oxygen-doped graphitic carbon nitride and zeolite (H-ZSM-5) composite (O−g−C_3N_4/H-ZSM-5) was synthesized using hydrogen peroxide and urea as the oxygen and g−C_3N_4 precursors, respectively, and perlite as the zeolite source, via calcination at 550 °C. BET N_2 adsorption-desorption analysis verified that the 40%O−g−C_3N_4/H-ZSM-5 composite had a high surface area of 259.13 m^2/g with mesopores and micropores, and X-ray photoelectron spectroscopy (XPS) confirmed the existence of the O atom in the g−C_3N_4 framework. The obtained O−g−C_3N_4/H-ZSM-5 catalyst showed excellent photocatalytic performance for the photodegradation of RR 195, approximately 96.6% with a high rate constant of 0.1167 min^{-1} under solar light irradiation without the use of H_2O_2. It also exhibited remarkable stability and long-term recyclability, with the photodegradation efficiency of RR 195 above 91%. In conclusion, the O−g−C_3N_4/H-ZSM-5 composite photocatalyst is suitable for numerous applications in the field of the photocatalytic degradation of organic pollutants.

1. Introduction

Currently, environmental pollution, particularly dye waste from the textile industry, is a global concern. Consequently, many methods have been used to remove these dyes [1, 2], of which, the photocatalytic method has attracted considerable attention because of its many advantages, such as rapid treatment rate and high efficiency. Photocatalysis occurs under the simultaneous action of catalysts and light [3]. Titanium dioxide (TiO_2) is a widely used photocatalyst, however, it possesses high band gap energy from 3 to 3.2 eV, only using a maximum of 5% solar energy [4]. Recently, zinc oxide (ZnO) with the same band gap energy range as TiO_2 has attracted more attention because of its unique photocatalytic applications stemming from its high thermal stability and low production cost [5, 6]. Unfortunately, the issues of the high band gap energy and high recombination of the photogenerated e^-/h^+ pairs, particularly at the nanoscale, have limited the photocatalytic efficiency [7]. Hence, scientists have attempted to identify new materials with relatively low band gap energy, high surface area, high durability, and ease of fabrication on a large scale, which can operate in visible light.

Among the new materials, g−C_3N_4, an organic polymeric semiconductor, has become important because of its unusual theoretical predictions of properties and potential applications. Chen et al. [8] investigated the structure of mesoporous C_3N_4 showing that it has a large surface area, uniform pore size with a 2D framework, and optical ability under visible light. Meada et al. [9] demonstrated the photocatalytic activity of g−C_3N_4 in the decomposition of water to H_2 through reduction or O_2 through oxidation under visible light. Thomas et al. [10] evaluated the structure of g−C_3N_4 with the changes in the structure and morphology as well as using it as a nonmetallic catalyst. Indeed, g−C_3N_4 is less toxic, cheap, and easy to synthesize, as it has a narrow band gap energy (approximately 2.7 eV) [11–16]. Hence, with good safety and chemical stability, g−C_3N_4 has been used in photocatalysis to decompose many toxic organic compounds in water, however, it has relatively low photocatalytic performance due to weak light absorbability along with the fast recombination rate of the e^-/h^+ pairs. Many methods have been proposed to modify g−C_3N_4 to overcome these issues, including the synthesis of porous g−C_3N_4 [17], a combination of g−C_3N_4 and other materials through doping or grafting

* Corresponding author.
E-mail address: phamxuannui@humg.edu.vn (X.N. Pham).

https://doi.org/10.1016/j.jtice.2020.09.018
1876-1070/

techniques [18, 19], or more particularly, the formation of composite materials [20-22].

Doping is useful to tune the electronic structure of g–C_3N_4 and further improve its light absorbability, as well as creating many defects in the g–C_3N_4 framework, which act as "*electron traps*," leading to limited recombination of the e^-/h^+ pairs, thereby increasing the photocatalytic activity of g–C_3N_4. For instance, a new porous intramolecular g-C_3N_4-based donor-acceptor conjugated copolymer was synthesized by copolymerizing urea with MF resin [23]. The nanocomposite of carbon quantum dots (CQDs), such as g-C_3N_4 QDs/$BiVO_4$ Z-scheme nanoheterostructure [24] and CQDs@MIL-125(Ti) photocatalyst [25] are highly efficient photocatalysts for the degradation of tetracycline (TC) under visible light irradiation. Zhang et al. [26] synthesized potassium-doped graphitic carbon nitride (K–C_3N_4) for the degradation of phenol and MB, and $[WO_4]_2$-doped g–C_3N_4 nanosheets enhanced the efficiency of visible light irradiation [27]. Surendar et al. [28] reported that the photocatalytic activity of Fe-doped g–C_3N_4 nanosheets is almost seven times higher than that of bulk g–C_3N_4. Vasudha et al. [29] utilized the one-pot precipitation method to synthesize a novel complex of Ag/AgI/WO_3 heterojunction-anchored P and S co-doped g–C_3N_4 as a dual Z-scheme photocatalyst for dye degradation. Yangang et al. [30] synthesized Zr-doped g–C_3N_4 to study the degradation of Rhodamine B (RhB) under simulated solar light irradiation. Recently, g–C_3N_4 has been doped by non-metal elements such as O, C, P, and S. Liu et al. [31] reported the simultaneous (S, P, and O) doping and exfoliation of g–C_3N_4 into ultrathin 2D nanosheets by an annealing method. Oxygen self-doped g–C_3N_4 with a tunable electronic band structure via ambient air exposure has been used as the photocatalyst for RhB photodegradation [32]. A hierarchically porous g–C_3N_4 tube oxygen-doped by thermal oxidation exfoliation at 600 °C prepared by Yu et al. [33] also showed a narrow band gap of 2.61 eV. Undeniably, the doping of g–C_3N_4 with non-metal elements is becoming a new research field for the design and preparation of more effective visible light photocatalysts.

Aluminosilicate zeolite, particularly H-ZSM-5, is an ideal support because of its large surface area, good thermal and mechanical stability, great adsorption ability, and shape-selective properties. Moreover, H-ZSM-5 is a suitable supporting catalyst in photodegradation due to its potential to facilitate the reactions of the photogenerated charge carriers and decrease the electron-hole recombination rate [34, 35]. Kiros et al. [36] tested TiO_2 supported on zeolite Y for the textile wastewater in Ethiopia, showing that it exhibited a 20 times higher mass-normalized turnover rate than that of pristine TiO_2. A novel H-ZSM-5 zeolite nanorod-decorated g–C_3N_4 prepared by Prakash et al. [37] degraded more than 99% and 98% of the RhB and CV dyes, respectively.

In the present study, we developed a green synthesis method for the fabrication of an O–g–C_3N_4/H-ZSM-5 composite derived from expanded perlite using H_2O_2 for the formation of the O-containing species in the g-C_3N_4 bulk. The photocatalytic activity of the O–g–C_3N_4/H-ZSM-5 composite was investigated for the photodegradation of RR 195, reaching 96.6% under solar light and ambient conditions. The kinetic models for the photodegradation of RR 195 by O–g–C_3N_4/H-ZSM-5 and the reusability of this catalyst were studied.

2. Experimental

2.1. Materials

Raw perlite was obtained from the Yenbai province, Vietnam, with a chemical composition of 68.51% SiO_2, 0.35% TiO_2, 14.54% Al_2O_3, 3.52% FeO, 0.09% MnO, 1.04% MgO, 2.71% CaO, 3.6% Na_2O, 4.29% K_2O, 0.07% P_2O_5, and 0.69% loss in ignition (LOI). All chemical reagents of the highest available purity, including tetra-propylammonium hydroxide (TPAOH, 25%), H_2O_2, NaOH, H_2SO_4, NH_4Cl, urea, and RR 195 were supplied by Sigma-Aldrich and used as received without further purification.

2.2. Synthesis of materials

2.2.1. Synthesis of H-ZSM-5 zeolite

The synthesis of H-ZSM-5 zeolite was a two-step process. In the first step, the raw perlite was washed several times with distilled water, dried overnight at 90 °C, crushed and sieved with a 180-mesh sieve, then thermally activated at 900 °C for 3 h to obtain the expanded perlite (EP) and had a SiO_2/Al_2O_3 molar ratio of 8.05. EP was used as the only aluminum source, and sodium silicate was used as the supplementary Si source for the synthesis of ZSM-5.

ZSM-5 zeolite was prepared via a hydrothermal crystallization method. In a typical synthesis, the calculated amounts of EP and NaOH were dissolved in distilled water at 80 °C. After 30 min of homogenization, TPAOH was added and stirred for 60 min. The pH of the mixture was adjusted to 10 using H_2SO_4 under vigorous stirring. The composition of the mother liquor was as follows: Si/Al molar ratio of 50, H_2O/SiO_2 ratio of 40, $NaOH/SiO_2$ ratio of 0.26, and TPAOH/SiO_2 ratio of 0.25. Finally, the gel formed was placed in Teflon-lined stainless-steel autoclaves and crystallized using a thermal treatment at 180 °C for 48 h. The solid product was washed with distilled water, dried at 100 °C overnight, and calcined in air at 550 °C for 5 h at the heating rate of 5 °C/min. The zeolite obtained in Na-type ZSM-5 was treated with a 1.0-N solution of NH_4Cl at 80 °C for 8 h to exchange its cations with ammonium ions. The H^+ ion-exchanged ZSM-5 (H-ZSM-5) zeolite was obtained by calcination at 500 °C for 5 h.

2.2.2. Synthesis of O-doped graphitic carbon nitride (O–g–C_3N_4)

Urea was used as a precursor for graphitic carbon nitride (g–C_3N_4) nanosheets, and the doping oxygen was supplied by hydrogen peroxide. In a typical synthesis, 9 g of urea was dispersed in 40 mL of H_2O_2, and the mixture was stirred for 15 min at room temperature. Next, the slurry was dried at 60 °C for 12 h to recrystallize the urea. The final product was obtained after calcination at 550 °C for 2 h at the heating rate of 2 °C/min and denoted as O–g–C_3N_4. Moreover, 9 g of urea was heated at 550 °C for 2 h at the heating rate of 2 °C/min and called g–C_3N_4.

2.2.3. Synthesis of O–g–C_3N_4/H-ZSM-5 composite

First, the calculated amount of H-ZSM-5 zeolite was added to 9 g of urea in 40 mL of H_2O_2, the mixture was stirred for 30 min at room temperature, before the slurry was dried at 60 °C for 12 h to recrystallize the urea. The final product was obtained after calcination at 550 °C for 2 h at the heating rate of 2 °C/min. The O–g–C_3N_4 mass content in the O–g–C_3N_4/H-ZSM-5 composite ranged from 30 wt.% to 50 wt.% with respect to O–g–C_3N_4, and the corresponding samples were named 30%O–g–C_3N_4/H-ZSM-5, 40%O–g–C_3N_4/H-ZSM-5, and 50%O–g–C_3N_4/H-ZSM-5, respectively.

Conventional g–C_3N_4/H-ZSM-5 was prepared following the same procedure described above, but without the addition of H_2O_2 and denoted as g–C_3N_4/H-ZSM-5.

2.3. Characterizations

The crystal lattice structure of the synthesized samples was determined by X-ray powder diffraction (XRD) using a D8 ADVANCE system (Cu Kα_1 copper radiation, $\lambda = 0.154$ nm, 3° min^{-1} scanning speed, Bruker, Germany). Surface morphology was observed by a scanning electron microscope (S-4800, Hitachi). The Fourier transform infrared spectra (FT–IR) were measured with an FTIR Affinity-1S (SHIMADZU). X-ray energy dispersion (EDX) and EDX mapping were performed with a JED-2300 with a gold coating. The UV–vis diffuse reflectance (DRS-UV) and photoluminescence (PL) spectra were recorded with the UV-2600 spectrophotometer (Shimadzu) and the Cary Eclipse fluorescence spectrophotometer (Varian), respectively. Furthermore, the Brunauer–Emmett–Teller (BET) specific surface area was determined at liquid-nitrogen temperature (77 K) using the N_2

adsorption-desorption technique on a ChemBET-3030 system. Also, X-ray photoelectron spectroscopy (XPS) was conducted using an ESCALab 250 spectrometer (Thermo VG, UK). Photocurrent analyses were conducted on an electrochemical analyzer (CHI660B Instrument) in a standard three-electrode system, with Ag/AgCl and a saturated calomel electrode used as a counter electrode and a reference electrode, respectively. The electrolyte was an aqueous solution of 1 M Na_2SO_4. The photoelectrochemical response current of the samples was measured by the static potential method, the voltage applied to the working electrode was 1.5 V. Each cycle on or off was 30 s and the total time was 360 s. The working electrode was prepared as follows: 0.1 mL of sample slurry (0.5 gmL^{-1}) was drop-casted onto a piece of FTO slice with a fixed area of 0.283 cm^2, which was dried at 80 °C for 1 h.

2.4. Photocatalytic activity of photocatalysts

The photocatalytic activity of the materials was evaluated using RR-195 in an aqueous solution with solar irradiation at room temperature. In the experiment, 50 mg of the photocatalysts were dispersed in the RR 195 solution (40 mL, 50 ppm). Prior to sunlight irradiation, the mixture was magnetically stirred for 60 min to achieve the adsorption-desorption equilibrium. At fixed time intervals, 5-mL samples were taken and centrifuged to remove the solids. The supernatant was analyzed by recording the variation in the absorption peak position (541 nm for RR-195) using a UV–Vis 2450 spectrometer. The RR 195 concentration at the equilibrium was taken as the initial concentration (C_o) for the RR 195 photocatalytic degradation.

To detect the reactive oxidative species produced in the photocatalytic process, tert-butyl alcohol (TBA), 1,4-benzoquinone (BQ), ammonium oxalate monohydrate (AO), and potassium dichromate ($K_2Cr_2O_7$) were used to capture $^{\bullet}OH$, $^{\bullet}O_2^-$, h^+, and ē, respectively [38]. The experimental steps were similar to the above photocatalytic activity test, with 1 mmol of scavenging agents added to the reaction solution at the beginning of solar light irradiation.

The degradation experiments were conducted under solar irradiation in the third week of May 2019 for the RR 195 degradation. The sunlight intensity was measured with a pyranometer, USA, with average solar flux (700 lx).

3. Results and discussion

3.1. Photocatalyst characterization

The crystalline structure and phase of the photocatalyst samples were characterized by XRD. As shown in Fig. 1, the XRD patterns of pure g–C_3N_4 and O–g–C_3N_4/H-ZSM-5 composites showed diffraction peaks identified at 13.2° and 27.3° corresponding to the (100) and (002) planes of the crystal faces of g–C_3N_4, respectively (JCPDS 87–1526) [39]. The diffraction peak at 13.2° corresponded to the in-plane structural packing motif of tri-s-triazine units, and the typical (002) plane corresponded to the interlayer stacking of the conjugated aromatic systems [40]. However, for pure O–g–C_3N_4 and O–g–C_3N_4/H-ZSM-5 composites, the peak at 27.3° broadened and shifted significantly toward a larger 2θ value and the peak at 13.2° disappeared, indicating that O–g–C_3N_4 had a considerably smaller crystal size than that pure g–C_3N_4 and that crystal lattice distortion arose from the defects in the g–C_3N_4 network when C or N was substituted with O [41]. In contrast, the characteristic XRD peaks of H-ZSM-5 zeolite were observed at 2θ = 7.87°, 9.07°, 13.63°, 14.39°, 15.34°, 15.81°, 23.37°, 24.36°, 25.73°, and 30.24°, which corresponded to the (101), (111), (102), (112), (131), (022), (051), (313), (323), and (062) planes, respectively (JCPDS 89–1421) [42]. The XRD patterns of g–C_3N_4/H-ZSM-5 and O–g–C_3N_4/H-ZSM-5 composites showed that the intrinsic lattice structure of zeolite was preserved, confirming that anchoring g–C_3N_4 on the H-ZSM-5 did not disturb the lattice structure of zeolite. Remarkably, the intensity of the peaks in O–g–C_3N_4/H-ZSM-5 became weaker than in g–C_3N_4/H-ZSM-5, suggesting that the O–g–C_3N_4/H-ZSM-5 samples had a considerably smaller crystal size than g–C_3N_4/H-ZSM-5. The average crystalline size of composite powders was determined using the Debye–Scherrer's equation:

$$D = \frac{k\lambda}{\beta\cos\theta} \quad (1)$$

where D is the crystalline size, k is a shape factor, which is typically 0.89, λ is the Cu Kα radiation wavelength (λ = 1.54Å), β is the line broadening at half the maximum intensity, and θ is the diffraction angle. The crystalline size was calculated for the (101) reflection plane and the average grain size of g-C_3N_4/H-ZSM-5 and O-g-C_3N_4/H-ZSM-5 was 35.68 and 20.07 nm, respectively. Additionally, the diffraction peak was shifted slightly to the lower 2θ region, which could be attributed to the chemical interaction between H-ZSM-5 and g–C_3N_4.

In contrast, the XRD patterns of the x–O–g–C_3N_4/H-ZSM-5 samples (Fig. 1(b)) indicated that the peak intensity changed with an increase in the amount of O–g–C_3N_4. Herein, the 50%O–g–C_3N_4/H-ZSM-5 sample exhibited weaker peak intensity than the 30% and 40%O–g–C_3N_4/H-ZSM-5 samples, confirming that the crystals of O–g–C_3N_4/H-ZSM-5 were downsized with an increase in the number of O-doped-g–C_3N_4 nanosheets.

To further determine the chemical structure of H-ZSM-5, the g–C_3N_4, O–g–C_3N_4, and composite samples were investigated using

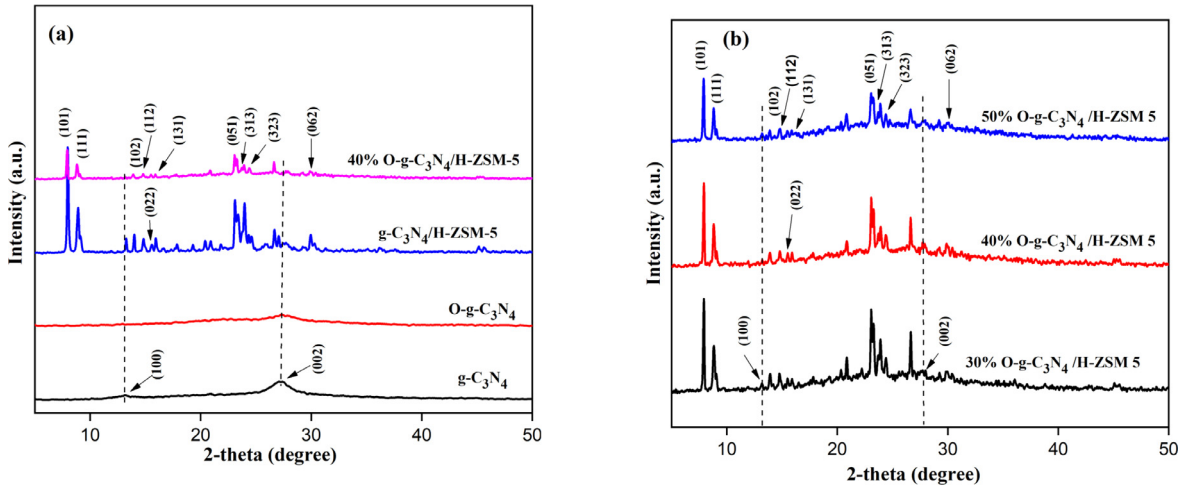

Fig. 1. XRD patterns of (a) g-C_3N_4, O-g-C_3N_4, g-C_3N_4/H-ZSM-5 and (b) 30–50%O-g-C_3N_4/H-ZSM-5 samples.

FT–IR spectra (Fig. 2). The broad absorption band from approximately 3100 to 3300 cm^{-1} was assigned to the stretching vibration of the primary ($-NH_2$ groups) and secondary (=NH groups) amines and their intermolecular hydrogen bonding interactions or surface hydroxyl groups [43, 44]. The absorption bands at 1574 and 1638 cm^{-1} were assigned to the C = N stretching vibration mode [45, 46]. The characteristic peaks at 1238, 1317, and 1458 cm^{-1} corresponded to the stretching vibration bands of the C–N heterocycle [47]. The peaks that appeared at 810 and 891 cm^{-1} could be attributed to the characteristic breathing vibration of the triazine unit [48]. Compared with pure g–C_3N_4, new bands in the spectra of O–g–C_3N_4 and O–g–C_3N_4/H-ZSM-5 at 1242 cm^{-1} could be assigned to the stretching vibration absorption of the C–O–C group [49]. In the FT–IR spectra of H-ZSM-5, the characteristic absorption band at 546 cm^{-1} appeared, indicating the formation of the double five-ring (D_5R) by the tetrahedral SiO_4 and AlO_4 units [50]. The region around 789 cm^{-1} corresponded to the symmetric stretching of the Si–O–Si group, while the band around 1049 cm^{-1} was attributed to the asymmetric stretching vibration of the Si–O–T group from the intra-tetrahedral mode of the zeolite framework [51]. The main characteristic peaks of H-ZSM-5 zeolite and g-O-C_3N_4 appeared in the O-g-C_3N_4/H-ZSM-5 composite (Fig. 2(a)), with the main characteristic peaks of Si-O and Al-O stretching vibrations in the H-ZSM-5 zeolite structure and the peak intensities of O-g-C_3N_4 decreasing with slight shifts to lower wavenumbers in the g-O-C_3N_4/H-ZSM-5 composite. This indicates the coexistence of the O-g-C_3N_4 and H-ZSM-5 zeolite in the composite, and the O-doped g-C_3N_4 was well incorporated in the H-ZSM-5 zeolite. The obtained XRD results also support this structure.

The specific surface area and the pore size of H-ZSM-5, O–g–C_3N_4, and the 40%O–g–C_3N_4/H-ZSM-5 composite were determined using the N_2 adsorption-desorption isotherms and BJH pore size distribution, as shown in Fig. 3. The specific surface area, pore volume, and the pore size distribution of the samples are summarized in Table 1. The BET specific surface area of the pristine H-ZSM-5 was 286.03 m^2g^{-1}. Compared with the pristine H-ZSM-5, the O–g–C_3N_4/H-ZSM-5 composite exhibited a slightly lower specific surface area of 259.13 m^2g^{-1}. Meanwhile, the average pore size distribution of the synthesized O–g–C_3N_4/H-ZSM-5 composite increased from 2.46 nm for H-ZSM-5 to 9.95 nm. This was attributed to the presence of the O–g–C_3N_4 coating on the surface of the H-ZSM-5 that led to a reduction in the surface area, however, the presence of O-doped g–C_3N_4 also offered many more porous structures,

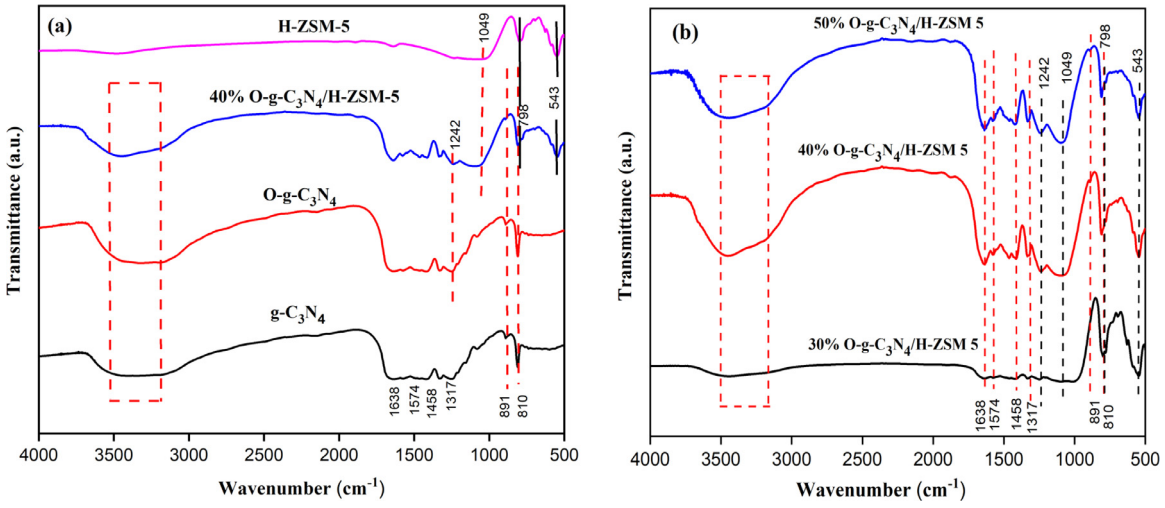

Fig. 2. FT-IR spectra of (a) g-C_3N_4, O-g-C_3N_4, g-C_3N_4/H-ZSM-5 and (b) 30–50%O-g-C_3N_4/H-ZSM-5 samples.

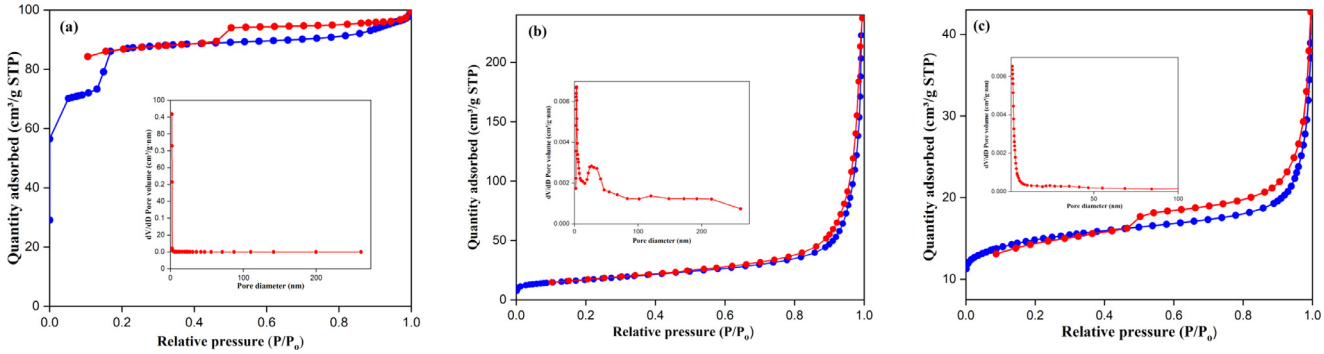

Fig. 3. N_2 adsorption-desorption isotherms and the corresponding pore size distribution curvet (inset) of (a) H-ZSM-5, (b) O-g-C_3N_4 and (c) 40%O-g-C_3N_4/H-ZSM-5 composite.

Table 1
Measured BET parameters of H-ZSM-5, O-g-C_3N_4 and O-g-C_3N_4/H-ZSM-5 composite.

Sample	Surface area (m^2g^{-1})	Pore volume ($cm^3.g^{-1}$)	Average pore size (nm)
H-ZSM-5	286.03	0.15	2.46
O-g-C_3N_4	58.20	0.37	30.70
40%O-g-C_3N_4/H-ZSM-5	259.13	0.15	9.95

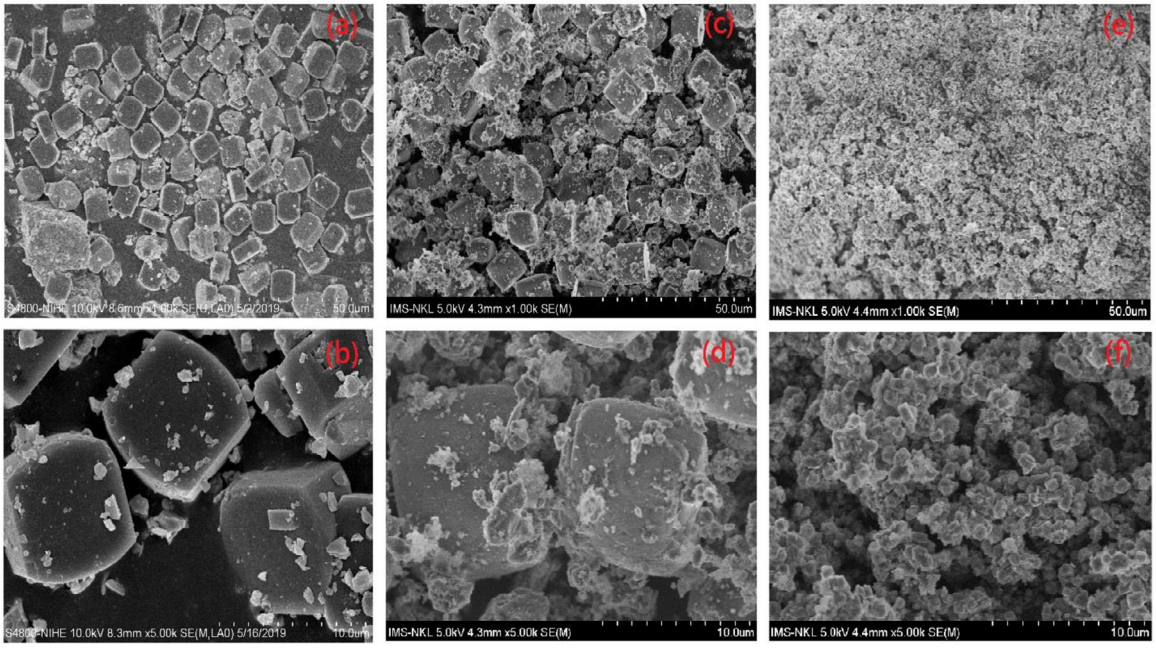

Fig. 4. SEM images of H-ZSM-5 (a, b), g-C_3N_4/H-ZSM-5 (c, d), and 40%O-g-C_3N_4/H-ZSM-5 (e, f) nanocomposite.

contributing to the improvement in the pore size. Hence, the relatively large specific surface area along with the increased pore size could facilitate the adsorption of the pollutants to the active sites in the pores for excellent photocatalytic performance.

The surface morphology of the H-ZSM-5 zeolite, g–C_3N_4/H-ZSM-5, and 40%O–g–C_3N_4/H-ZSM-5 composites was analyzed using SEM. As shown in Fig. 4(a) and (b), the pristine H-ZSM-5 displayed the spherical and cubic shapes of the zeolite crystal. The g–C_3N_4/H-ZSM-5 composite was irregular with a rough surface structure, as shown in Fig. 4(c) and (d). From the SEM micrographs of the O–g–C_3N_4/H-ZSM-5 composite (Fig. 4(e) and (f)), it was inferred that the cubic H-ZSM-5 zeolite was immobilized onto the matrix of the O-doped g–C_3N_4. The composite had good dispersion with a relatively smooth surface, and the morphology of the crystals was regular.

The elemental composition of the 40%O–g–C_3N_4/H-ZSM-5 sample was also confirmed by EDX analysis (Fig. 5(a)). Six main elements were observed, namely carbon (C), nitrogen (N), oxygen (O), sodium (Na), aluminum (Al), and silicon (Si), corresponding to the various positions of 0.2, 0.4, 0.5, 1.0, 1.5, and 1.8 keV, respectively, with the O element occupying the largest mass of up to 51.62%. No other elements were detected suggesting that the 40%O–g–C_3N_4/H-ZSM-5 sample was rather pure. From the results of the elemental mapping of the Si, Al, O, Na, C, and N elements (Fig. 5(b–g), these elements were uniformly distributed on the surface of the 40%O–g–C_3N_4/H-ZSM-5 sample.

The surface chemical composition of the 40%O–g–C_3N_4/H-ZSM-5 sample was confirmed by the surface survey and high-resolution XPS analysis (Fig. 6). The presence of the C, N, and O elements in the composite (Fig. 6(a)) confirmed the incorporation of O-doped g–C_3N_4 into the H-ZSM-5 zeolite structure. In the high-resolution spectrum of C 1 s (Fig. 6(b)), the peak at 284.79 eV originated from the adventitious-type carbon (sp^3 C–C). The peaks at 286.1 eV and 288.01 eV corresponded to the C–NH_2 and N = C–N of the CN units, respectively [52, 53]. As shown in high-resolution C 1 s spectra, the new peak at a binding energy of 289.1 eV corresponding to N—C—O binds appeared in the C 1 s spectrum of O-g-C_3N_4/H-ZSM-5 sample, which is consistent with the assumption that O atoms are doped into the g-C_3N_4 heterocycles by bonding with C atoms, which was also confirmed by the FT-IR analysis. The presence of the C–O and N—C—O bonds in the O-doped g–C_3N_4 showed that the O atoms could be directly bonded to the sp^2-hybridized carbon in the composite [54, 55]. In the high-resolution spectrum of N 1 s (Fig. 6(c)), three peaks corresponded to 398.5 eV, 399.8 eV, and 401.1 eV, respectively, and could be assigned to the tertiary nitrogen N–$(C)_3$, C–N = C in the aromatic CN heterocycles, and the surface amino group (C–NH_2) moiety in the CN framework, respectively [56, 57]. In addition, the O 1 s spectrum (Fig. 6(d)) showed a characteristic peak binding energy at 532.59 eV due to water adsorption (–OH hydroxyl groups), and 533.06 eV was ascribed to the (O–N) oxygen. Again, a new peak at the binding energy of 531.4 eV corresponding to the N—C—O bonds appeared in the O 1 s, further confirming that the O atoms were doped in the matrix of g–C_3N_4 by bonding with the C atoms.

The optical absorption property considerably influenced the photocatalytic activity of the catalyst, thus, the absorption properties of the as-prepared samples were investigated using UV–vis diffuse reflection spectra (DRS), and the results are shown in Fig. 7(a). The UV–vis spectra show the absorption edge of the g–C_3H_4 red-shifts from 440 nm to 465 nm after O doping. Compared with the pure g–C_3N_4, the O-doped g–C_3N_4 exhibited more intense absorption in the broad region of 200–600 nm. The optical band-gap energy of the samples was estimated by the following Kubelka–Munk equation (1a):

$$\alpha h\nu = A\left(h\nu - E_g\right)^{n/2} \quad (1a)$$

where E_g is the band-gap energy of the semiconductor, A is the absorption constant, h is Planck's constant, and α and νrepresent the absorption coefficient and the light frequency, respectively. The value of n was determined by the transition mode of the semiconductor. According to previous studies [58], an n value of 1 allows direct electronic transitions. Further, the band-gap energies of the pure g–C_3N_4, O–g–C_3N_4, and O–g–C_3N_4/H-ZSM-5 samples were obtained from a plot of $(\alpha h\nu)^{1/2}$ versus $h\nu$ (Fig. 7(b–f)) as 2.79, 2.74, 2.72, 2.62, and 2.75 eV, respectively. The presence of O–g–C_3N_4 contributed to the red-shift of the absorption onset, resulting in the narrow band gap of the O–g–C_3N_4/H-ZSM-5 composite (Table 2).

To clarify the separation and recombination of the photoinduced excitons, the PL spectra of the pure g–C_3N_4, O–g–C_3N_4, and 30%–50%O–g–C_3N_4/H-ZSM-5 composites were investigated. As shown in Fig. 8(a), the PL emission peak for the pure g–C_3N_4 was at 449 nm and displayed the highest emission intensity, exhibiting

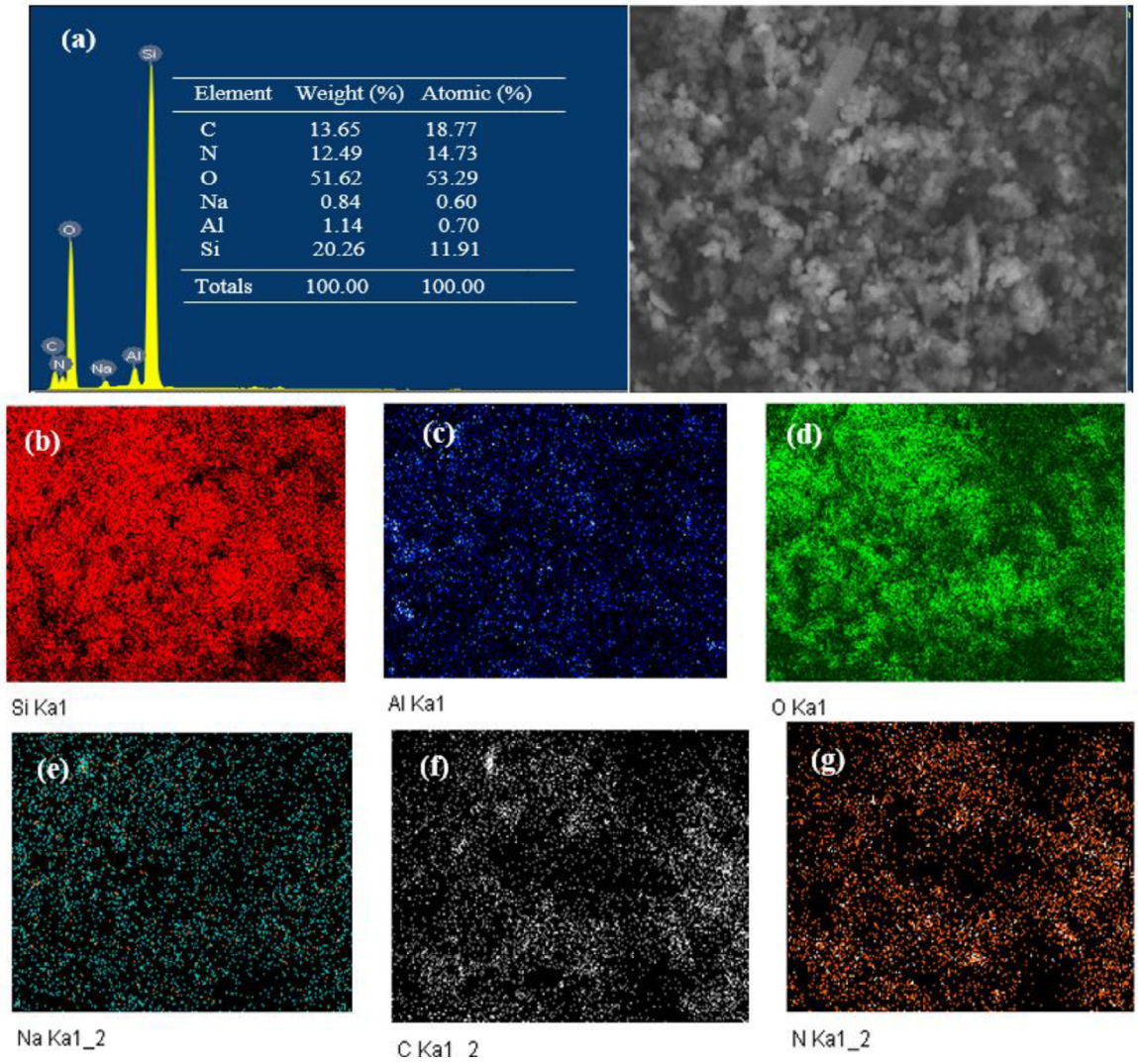

Fig. 5. (a) EDX spectrum and SEM micrograph with elemental mapping of (b) silicon, (c) aluminum, (d) oxygen, (e) sodium, (f) carbon and (g) nitrogen of the 40%O-g-C_3N_4/H-ZSM-5 composite.

rapid recombination of the electron-hole pairs. After the O-doped g–C_3N_4, the intensities of the PL spectra decreased, and the 40%O–g–C_3N_4/H-ZSM-5 exhibited the lowest PL emission peak. The reduction in intensity was in the following order: g–C_3N_4 > O–g–C_3N_4 > 50%O–g–C_3N_4/H-ZSM-5 > 30%O–g–C_3N_4/H-ZSM-5 > 40%O–g–C_3N_4/H-ZSM-5, implying that the highest separation efficiency of the photoexcited electron-hole pairs and the recombination of the electrons and the holes was effectively inhibited in the 40%O–g–C_3N_4/H-ZSM-5 composite. Moreover, the emission peak of the O-doped g–C_3N_4 samples showed a gradual red-shift, which was attributed to the narrowing of the band gaps for doping oxygen in g–C_3N_4 [59, 60].

To further clarify the separation and transfer feature of the photogenerated electron-hole pairs, the photocurrent response tests of as-synthesized g-C_3N_4, O-g-C_3N_4, and 30–50%O-g-C_3N_4/H-ZSM-5 were performed. The transient photocurrents were measured during a 400 s period in an on-and-off cycle mode as shown in Fig. 8(b), showing that 40%O-g-C_3N_4/H-ZSM-5 had a higher photocurrent density than 30%O-g-C_3N_4/H-ZSM-5, 50%O-g-C_3N_4/H-ZSM-5, O-g-C_3N_4, and g-C_3N_4, indicating more efficient separation of the photoinduced electron-hole pairs, which may be attributed to synergistic effects between O-g-C_3N_4 and H-ZM-5.

3.2. Photocatalytic activity test

3.2.1. Effect of H_2O_2 oxidizing agent on photodegradation of RR 195

The photocatalytic activity of the 40%O–g–C_3N_4/H-ZSM-5 catalyst was investigated during the photodegradation of RR 195 in the absence or presence of H_2O_2. As shown in Fig. 9, after 5 h of irradiation with solar light, approximately 98% of RR 195 was degraded in the presence of the H_2O_2, while approximately 96.6% of RR 195 was decomposed in the absence of H_2O_2. Thus, the photocatalytic activity of the 40%O–g–C_3N_4/H-ZSM-5 remained unchanged in the presence or the absence of H_2O_2. The incorporation of oxygen atoms effectively expanded the surface area, extended the solar light response, and improved the separation efficiency of the electron-hole pairs on the catalyst. This result also implied that the assistance of H_2O_2 was not needed for the degradation of RR 195 over the O-doped g–C_3N_4/H-ZSM-5 photocatalyst. This is a very beneficial photocatalytic activity.

3.2.2. Effect of different photocatalysts

The photocatalysis efficiency of the as-synthesized pure g–C_3N_4, O–g–C_3N_4, and 40%O–g–C_3N_4/H-ZSM-5 catalysts was investigated by degrading RR 195 under solar light. Fig. 10(a) shows that the initial

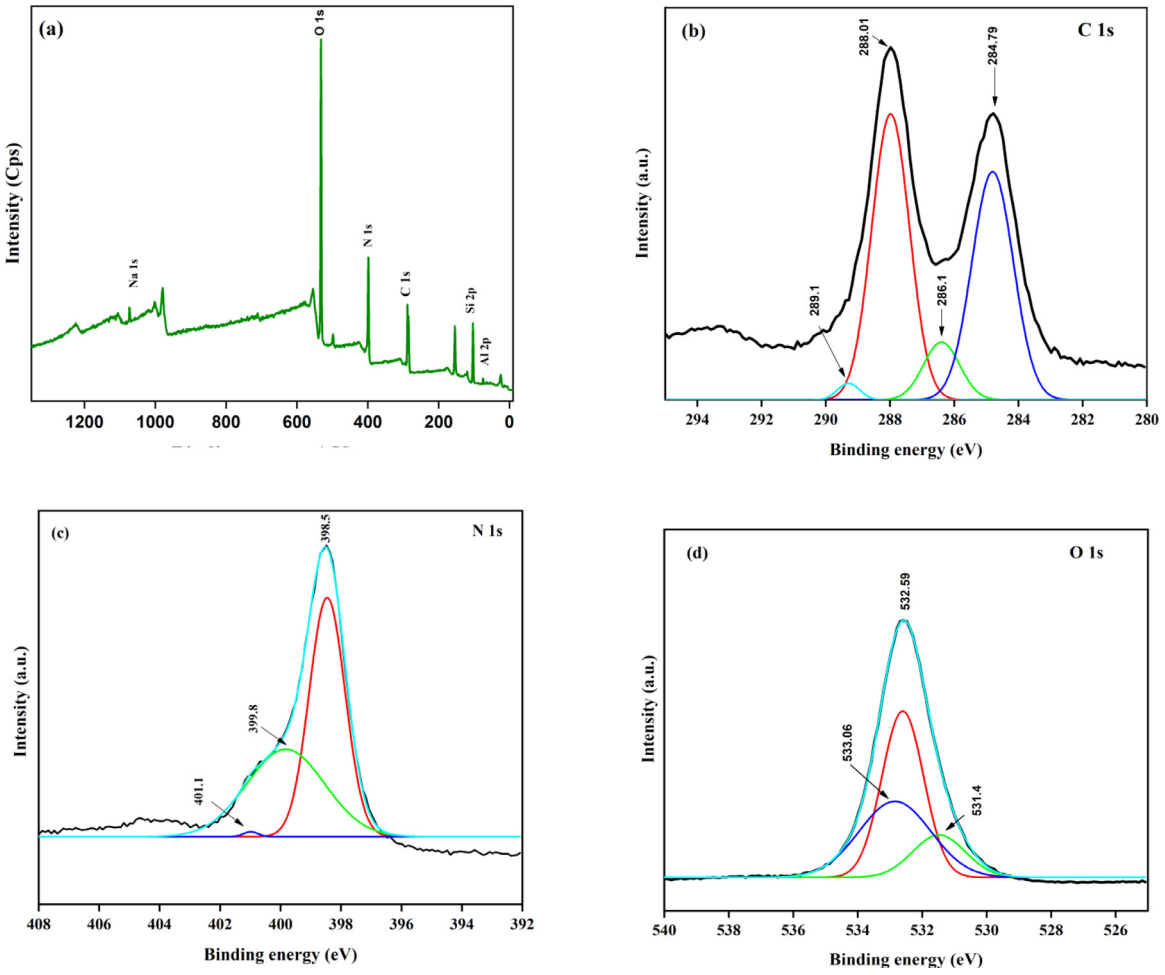

Fig. 6. (a) XPS survey spectra and high resolution (b) C 1 s, (c) N 1 s, and (d) O 1 s XPS spectra of 40%O-g-C_3N_4/H-ZSM-5 composite.

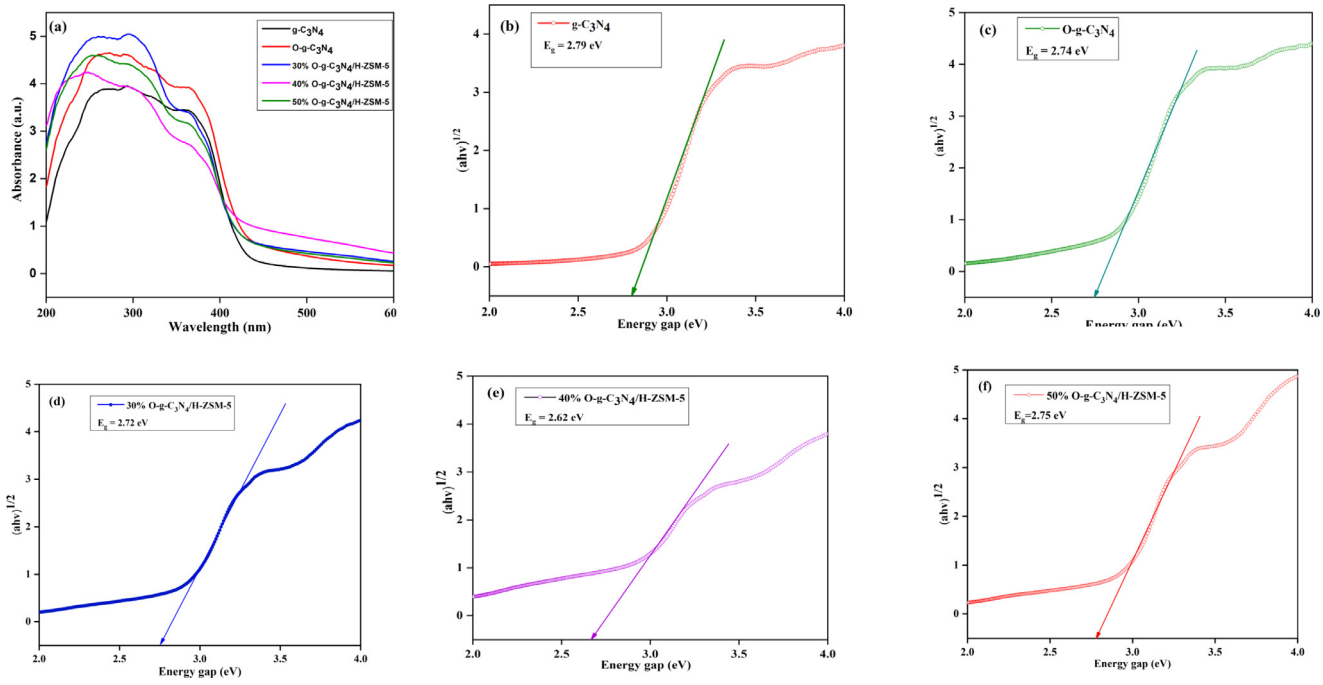

Fig. 7. (a) UV–vis diffuse reflectance spectra, and (b-f) Kubelka-Munk plot of g-C_3N_4, O-g-C_3N_4 and 30–50%O-g-C_3N_4/H-ZSM-5 composites.

Table 2
Optical properties of g-C_3N_4, O-g-C_3N_4 and the composite samples.

Sample	Absorption edge (nm)	Bandgap energy (eV)
g-C_3N_4	445	2.79
O-g-C_3N_4	453	2.74
30%O-g-C_3N_4/H-ZSM-5	456	2.72
40%O-g-C_3N_4/H-ZSM-5	473	2.62
50%O-g-C_3N_4/H-ZSM-5	451	2.75

adsorption rates of RR 195 over g–C_3N_4, O–g–C_3N_4, and 40%O–g–C_3N_4/H-ZSM-5 were 29.55%, 25.24%, and 24.13%, respectively. Compared with pure g–C_3N_4 and O–g–C_3N_4, the 40%O–g–C_3N_4/H-ZSM-5 composite exhibited relatively high photocatalytic performance in terms of the RR 195 degradation, and 96.56% of the RR 195 was degraded in 5 h under sunlight illumination, while 91.91% and 93.91% of RR 195 were degraded in 4 h over g–C_3N_4 and O–g–C_3N_4, respectively. Moreover, we observed that the photocatalytic efficiency tended to decrease after 5 h and was 90.90% for g–C_3N_4 and 92.67% for the O–g–C_3N_4 catalyst. This indicates that there is a recombination of photoinduced electron and holes, thus significantly decreasing the photocatalytic efficiency in the RR 195 degradation. Besides, the photocatalytic activity of the 40%g-C_3N_4/H-ZSM-5 composite was tested for the degradation of RR 195 dye under solar irradiation, showing that the RR 195 degraded better in the 40%g-C_3N_4/H-ZSM-5 and 40%O-g-C_3N_4/H-ZSM-5 composites than g-C_3N_4 and O-g-C_3N_4, 92.03% and 96.56% removal efficiency were obtained, respectively. These results indicate that the activity of the composite photocatalyst was due to the incorporation of O-doped g-C_3N_4 into the H-ZSM-5 zeolite structure and the role of H-ZSM-5 support increases the high migration efficiency of charge carriers and longer lifetime of separated electron-hole pairs derived from the formation of the heterojunction between the g-C_3N_4 and H-ZSM-5. Based on the obtained results, the enhancement of the photocatalytic activity of the 40%O–g–C_3N_4/H-ZSM-5 composite for the RR 195 degradation could be explained as follows. First, the better sunlight harvest ability of this composite system resulted in better photocatalytic degradation efficiency because more electron-hole pairs could be excited under the same sunlight irradiation conditions. Secondly, the crystal structure and the micro-morphology of the H-ZSM-5 catalyst support played a significant role in determining the photocatalytic efficiency for RR 195 degradation [61]. Thus, the obtained results well matched the analytical results from the BET surface area, UV–vis DRS, and PL spectra.

3.2.3. *Effect of O–g–C_3N_4 contents*

Further enhancements in photocatalytic efficiency were exhibited by the composite catalyst O–g–C_3N_4/H-ZSM-5, as a result of the synergetic effects between the photocatalytic active phase and the H-ZSM-5 support that increased sunlight absorption and efficiently separated the electron-hole pairs of the O–g–C_3N_4 on the support surface. Fig. 10(b) shows that the mass content of the O–g–C_3N_4 had a considerable influence on the photocatalytic activities of the composite, that is, the O–g–C_3N_4/H-ZSM-5 composite with 40 wt.% of O–g–C_3N_4 exhibited the highest photocatalytic activity, degrading 96.56% of RR 195 after 5 h of irradiation. In contrast, an O–g–C_3N_4 loading of more than 50 wt.% decreased the performance (86.99% degradation of RR 195 after 3 h of irradiation), as the excess O–g–C_3N_4 might form aggregates that block the transfer of electrons and holes in this system.

3.2.4. *Effect of photocatalyst dosage*

The influence of the different amounts of 40%O–g–C_3N_4/H-ZSM-5 catalyst was also investigated under the same reaction conditions. Fig. 10(c) shows that the highest photocatalytic efficiency was 96% after 5 h corresponding to 50 mg of the used catalyst, which decreased thereafter. A large amount of catalyst facilitated the formation of surface-active sites, leading to an improvement in the photocatalytic efficiency. However, if the amount of catalyst continually increased, the interaction among the outer layers of the catalyst material reduced the photon formation of the inner layers, which led to a decrease in the number of e^-/h^+ pairs as well as the photocatalytic efficiency [62].

3.2.5. *Effect of RR 195 concentration*

The initial concentration of the pollutant also affects the photodegradation activity, therefore, the degradation of RR 195 with different initial concentrations using the 40%O–g–C_3N_4/H-ZSM-5 photocatalyst was investigated, as shown in Fig. 10(d). When the initial concentration of RR 195 increased from 30 ppm to 90 ppm, the photocatalytic efficiency slightly decreased from 96.6% to 92.9%, implying that a high initial dye concentration could decrease the transmission opportunity and the path of the

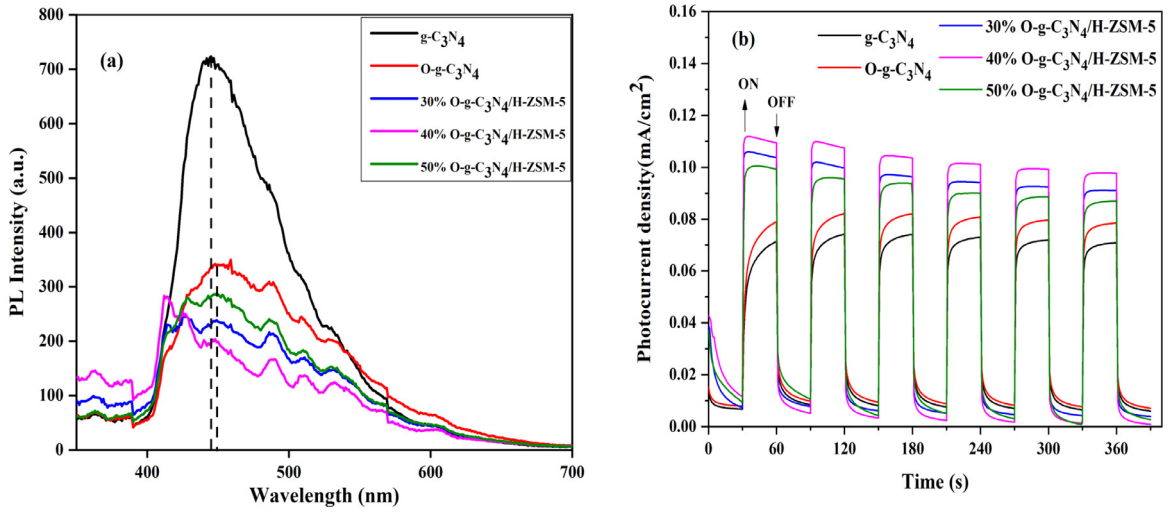

Fig. 8. (a) Photoluminescence spectra and (b) Transient photocurrent response of g-C_3N_4, O-g-C_3N_4, 30–50% O-g-C_3N_4/H-ZSM-5 composites.

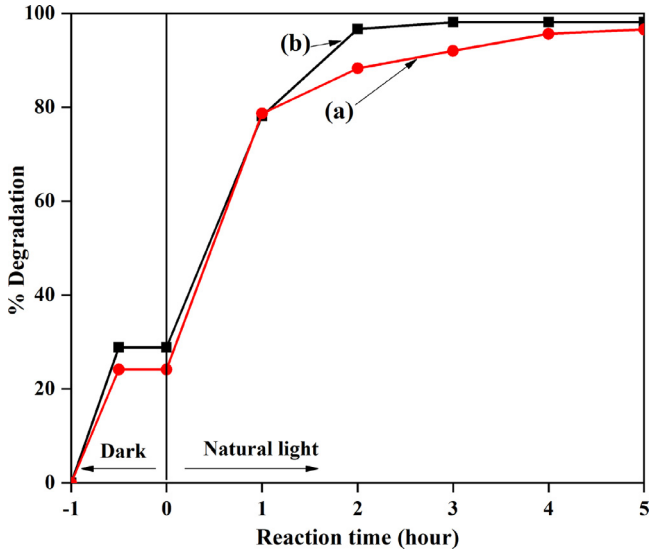

Fig. 9. Photodegradation of RR 195 over 40% O-g-C_3N_4/H-ZSM-5 photocatalyst (a) without of H_2O_2 and (b) with 1 mL of H_2O_2 as oxidizing agent (Reaction conditions: RR 195 concentration of 50 ppm, 50 mg of photocatalyst, natural light (=750 lx) and environment temperature (30 °C), pH = 6.5.

photon, thereby reducing the penetration rate of the solar light irradiation in the contaminant solution [63, 64].

The kinetics of the RR 195 photodegradation were modeled based on an operating temperature of 30 °C, 50 mg of the synthesized 40%O–g–C_3N_4/H-ZSM-5 catalyst, and a pH of 6.5, as shown in Eq. (1b):

$$-\ln\left(\frac{C_t}{C_o}\right) = k_p t \quad (1b)$$

where C_t and C_o are the concentrations at time t and time zero, respectively, and k_p is the first-order reaction rate constant (h^{-1}). As shown in Fig. 11(a), the linearity of the ln (C_o/C_t) versus irradiation time (t) plot suggested that the first-order reaction was not suitable for the photodegradation reaction, that is, the values of the regression coefficient (R^2) between 0.8 and 0.9 were not symptomatic of pseudo-first-order kinetics for the photodegradation of RR 195. In contrast, if the photodegradation process followed pseudo-second-order kinetics, the reaction equation could be represented as follows:

$$\frac{1}{C_t} - \frac{1}{C_o} = kt \quad (2)$$

where C_t and C_o are the concentration at time t and time zero, respectively, k is the pseudo-second-order reaction rate constant, and t is the irradiation time. The plot of $\left(\frac{1}{C_t} - \frac{1}{C_o}\right)$ versus t is shown in Fig. 11(b). We observed that the regression coefficient values for each concentration in the case of the pseudo-second-order kinetic model ($R^2 > 0.96$) were considerably higher than those of the pseudo-first-order kinetic model. The rate constant of the pseudo-second-order equation decreased from 0.1167 to 0.0512 min^{-1} when the initial concentration increased from 30 to 90 ppm. These results show that the photodegradation process was better represented by the pseudo-second-order model and that increasing the initial RR 195 concentration did not have a positive effect on the rate of the photodegradation process.

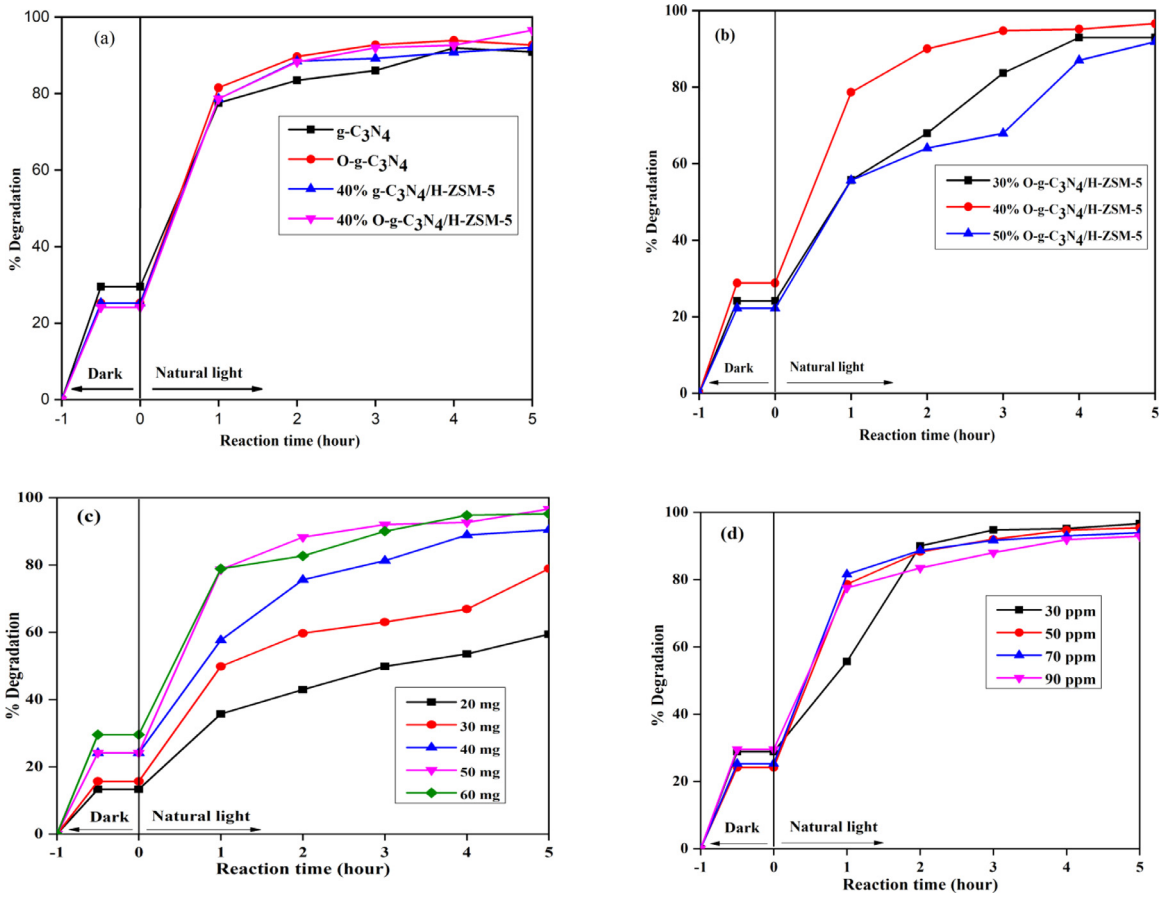

Fig. 10. Photodegradation of RR 195 under various reaction conditions of (a) photocatalysts, (b) mass contents of O-g-C_3N_4, (c) amount of photocatalysts, (d) concentration of the RR 195. Reaction conditions: solar light irradiation (=750 lx), environment temperature (30 °C), pH = 6.5.

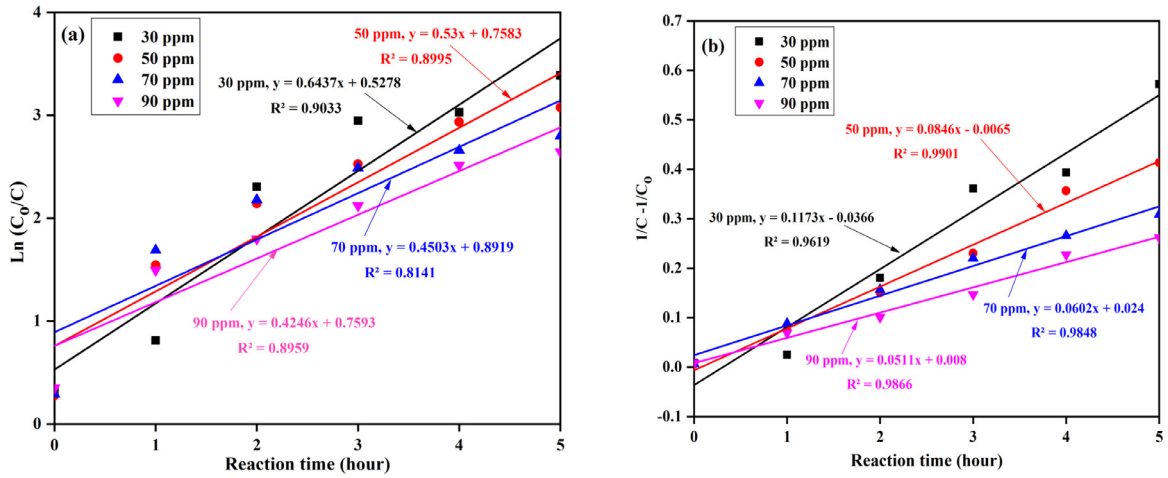

Fig. 11. Plot of (a) the pseudo-first order and (b) the pseudo-second order kinetic model for the photodegradation of RR 195 over 40%O-g-C_3N_4/H-ZSM-5 photocatalyst.

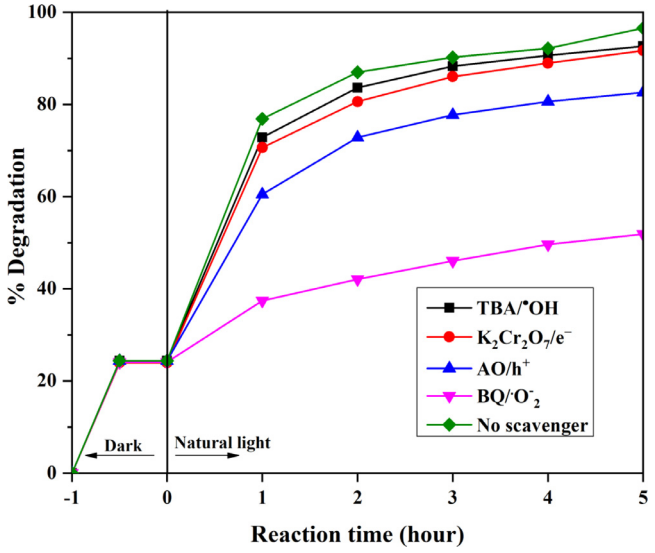

Fig. 12. The active species trapping experiments for degradation of RR 195 over 40%O-g-C_3N_4/H-ZSM-5 photocatalyst. Reaction conditions: solar light irradiation (=750 lx), environment temperature (30 °C), pH = 6.5.

3.3. Mechanism of photocatalytic activity

The quenching of radical species was performed to identify the reactive oxidative species participating in the photocatalytic degradation. The quenching agents, including TBA, Cr(VI), AO, and BQ were added into the 40%O-g-C_3N_4/H-ZSM-5 photocatalyst as hydroxyl radical ($^{\bullet}OH$) scavenger, electron ($\bar{e}$), holes (h^+) and superoxide radical ($^{\bullet}O_2^-$), respectively. As shown in Fig. 12, the photodegradation rate of RR 195 decreased from 92.41%, 91.68%, 82.38%, and 51.82% with the addition of TBA, Cr(VI), AO, and BQ into the reaction system, respectively. The efficiency of the photocatalytic degradation was slightly decreased after adding TBA and Cr(VI) compared with no scavenger, implying that $^{\bullet}OH$ and $\bar{e}$ do not play a major role in the photocatalytic activity. In contrast, when BQ and AO were added, there was a significant decrease in photocatalytic activity of RR 195, indicating that $^{\bullet}O_2^-$ and h^+ were produced in the photocatalytic process. The obtained results revealed that superoxide radicals and holes were mainly involved in the photocatalytic system, with the hydroxyl radical scavenger, electron having a lesser role in photodegradation [65-68].

In summary, the photocatalytic process involved the reactive oxygen species viz. the singlet oxygen and superoxide radical anions ($^{\bullet}O_2^-$), which were obtained by doping oxygen into g–C_3N_4. With the combined advantages of the high surface area of the H-ZSM-5 support with mesopores and micropores, wide visible light absorption range, high separation efficiency of the charge carriers, and the suitable band structure, the photodegradation mechanism of RR 195 over the O–g–C_3N_4/H-ZSM-5 composite can be explained as follows:

$$O-g-C_3N_4/\text{H-ZSM-5} + \text{sunlight irradiation} \rightarrow \bar{e}_{CB} + h^+_{VB} \quad (3)$$

$$\bar{e}_{CB} + O_2 \rightarrow {}^{\bullet}O^-_2 \quad (4)$$

$${}^{\bullet}O^-_2 + \text{RR 195} \rightarrow \text{mineralized products} \quad (5)$$

$$h^+_{VB} + \text{RR 195} \rightarrow \text{mineralized products} \quad (6)$$

3.4. Photocatalyst stability test

The recyclability and the photostability properties of the photocatalyst are very important for real-world applications. To evaluate the stability and the reusability of O-doped g–C_3N_4/H-ZSM-5, the reaction process of the synthesized 40%O–g–C_3N_4/H-ZSM-5 for RR 195 degradation was repeated four times. As shown in Fig. 13(A), the photocatalytic activity of this catalyst only slightly decreased (91.20% remaining) after four consecutive tests under the experimental conditions at which the optimal degradation rate was obtained. Moreover, the FT–IR spectra of the recycled 40%O–g–C_3N_4/H-ZSM-5 composite remained unchanged compared with the fresh sample (Fig. 13(B)). Besides, the XRD patterns (Fig. 13(C)) confirm that no obvious crystal structure changes occurred in the 40%O-g-C_3N_4/H-ZSM-5 catalyst after the fourth photodegradation cycle. These results demonstrate the excellent stability of the catalyst during photodegradation.

4. Conclusions

In conclusion, the O–g–C_3N_4/H-ZSM-5 photocatalyst, with excellent photocatalytic activity, was synthesized using expanded perlite and urea as precursors. The morphological, compositional, crystalline phase, textural nature, and optical properties of as-synthesized samples were characterized, demonstrating that 40%O-g-C_3N_4/H-ZSM-5 has the highest photocatalytic efficiency, with a photodegradation rate of up to 96.6% under solar light irradiation. The outstanding photocatalytic activity is attributed to the improved separation of

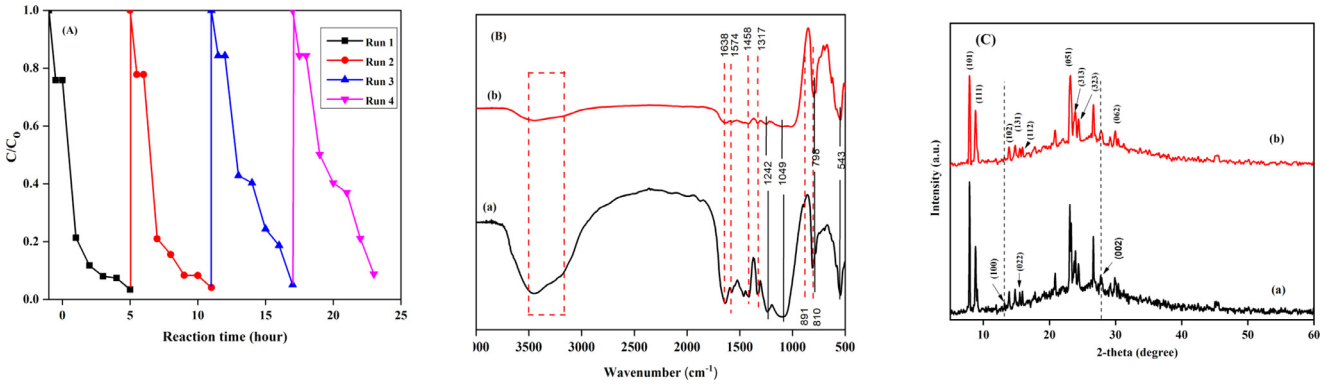

Fig. 13. (A) Cycling runs for the photodegradation of RR 195 over 40%O-g-C_3N_4/H-ZSM-5 composite, (B) FT-IR spectra, and (C) XRD patterns of (a) fresh and (b) used 40%O-g-C_3N_4/H-ZSM-5 photocatalyst. Reaction conditions: solar light irradiation (=750 lx), environment temperature (30 °C), pH = 6.5.

photoinduced charge carriers, the formation of a heterojunction between O-doped g-C_3N_4 and H-ZSM-5. Furthermore, $^{\bullet}O_2^-$ plays a major role in the photodegradation process. These findings provide new opportunities for the fabrication of efficient photocatalysts for the treatment of wastewater.

Declaration of Competing Interest

The authors declare that they have no known competing financial interests or personal relationships that could have appeared to influence the work reported in this paper.

Acknowledgments

This research was financially supported by the project of National Foundation for Science & Technology Development of Vietnam (No. 105.99-2018.301).

Supplementary materials

Supplementary material associated with this article can be found in the online version at doi:10.1016/j.jtice.2020.09.018.

References

[1] Fernández C, Larrechi MS, Callao MP. An analytical overview of processes for removing organic dyes from wastewater effluents. Trend Anal Chem 2010;29:1202–11.
[2] Yaseen DA, Scholz M. Textile dye wastewater characteristics and constituents of synthetic effluents: a critical review. Int J Environ Sci Technol 2019;16:1193–226.
[3] Chen X, Shen S, Guo L, Mao SS. Semiconductor-based photocatalytic hydrogen generation. Chem Rev 2010;110(11):6503–70.
[4] Devi LG, Kavitha R. A review on non-metal ion doped titania for the photocatalytic degradation of organic pollutants under UV/solar light: role of photogenerated charge support dynamics in enhancing the activity. Appl Catal B 2013;140–141:559–87.
[5] Hoffman AJ, Carraway ER, Hoffmann MR. Photocatalytic production of H_2O_2 and organic peroxides on quantum-sized semiconductor colloids. Environ Sci Technol 1994;28:776–85.
[6] Jang ES, Won JH, Hwang SJ, Choy JH. Fine tuning of the face orientation of ZnO crystals to optimize their photocatalytic activity. Adv Mater 2006;18:3309–12.
[7] Adnan MAM, Julkapli NM, Hamid SBA. Review on ZnO hybrid photocatalyst: impact on photocatalytic activities of water pollutant degradation. Rev Inorg Chem 2016;36(2):1–28.
[8] Chen X, Jun Y-S, Takanabe K, Maeda K, Domen K, Fu X, Antonietti M, Wang X. Ordered mesoporous SBA-15 type graphitic carbon nitride: a semiconductor host structure for photocatalytic hydrogen evolution-with visible light. Chem Mater 2009;21(18):4093–5.
[9] Maeda K, Wang X, Nishihara Y, Lu D, Antonietti M, Domen K. Photocatalytic activities of graphitic carbon nitride powder for water reduction and oxidation under visible light. J Phys Chem C 2009;113(12):4940–7.
[10] Thomas A, Fischer A, Goettmann F, Antonietti M, Müller J-O, Schlögl R, Carlsson JM. Graphitic carbon nitride materials: variation of structure and morphology and their use as metal-free catalysts. J Mater Chem 2008;18:4893–908.
[11] Li X, Zhang J, Shen L, Zou G. Preparation and characterization of graphitic carbon nitride through pyrolysis of melamine. Appl Phys A 2009;94(2):387–92.
[12] Stolbov S, Zuluaga S. Sulfur doping effects on the electronic and geometric structures of graphitic carbon nitride photocatalyst: insights from first principles. J Phys Condens Matter 2013;25:085507.
[13] Tahir M, Cao C, Butt FK, Butt S, Idrees F, Ali Z, Aslam I, Tanveer M, Mahmood A, Mahmood N. Large scale production of novel g-C_3N_4 micro strings with high surface area and versatile photodegradation ability. CrystEngComm 2014;16:1825–30.
[14] Wang X, Maeda K, Chen X, Takanabe K, Domen K, Hou Y, Fu X, Antonietti M. Polymer semiconductors for artificial photosynthesis: hydrogen evolution by mesoporous graphitic carbon nitride with visible light. J Am Chem Soc 2009;131(5):1680–1.
[15] Wang Y, Wang X, Antonietti M. Polymeric graphitic carbon nitride as a heterogeneous organocatalyst: from photochemistry to multipurpose catalysis to sustainable chemistry. Angew Chem Int Ed 2012;51(1):68–89.
[16] Mamba G, Mishra AK. Graphitic carbon nitride (g-C_3N_4) nanocomposites: a new and exciting generation of visible light driven photocatalysts for environmental pollution remediation. Appl Catal B 2016;198(5):347–77.
[17] Ding Z, Chen X, Antonietti M, Wang X. Synthesis of transition metal-modified carbon nitride polymers for selective hydrocarbon oxidation. Chem Sus Chem 2011;4(2):274–81.
[18] Liao G, Chen S, Quan X, Yu H, Zhao H. Graphene oxide modified g-C_3N_4 hybrid with enhanced photocatalytic capability under visible light irradiation. J Mater Chem 2012;22:2721–6.
[19] Cheng C, Shi J, Hu Y, Guo L. WO_3/g-C_3N_4 composites: one-pot preparation and enhanced photocatalytic H_2 production under visible-light irradiation. Nanotechnology 2017;28(16):164002.
[20] Wang Y, Shi R, Lin J, Zhu Y. Enhancement of photocurrent and photocatalytic activity of ZnO hybridized with graphite-like C_3N_4. Energy Environ Sci 2011;4:2922–9.
[21] Sun L, Zhao X, Jia C-J, Zhou Y, Cheng X, Li P, Fan LLW. Enhanced visible-light photocatalytic activity of g-C_3N_4-$ZnWO_4$ by fabricating a heterojunction: investigation based on experimental and theoretical studies. J Mater Chem 2012;22:23428–38.
[22] Yan P, Li D, Ma X, Xue J, Zhang Y, Liu M. Hydrothermal synthesis of Bi_2WO_6 with a new tungsten source and enhanced photocatalytic activity of Bi_2WO_6 hybridized with C_3N_4. Photochem Photobiol Sci 2018;17:1084–90.
[23] Huinan C, Chunbo L, Guangbo C, Guangfu L, Hongjun D, Chunxue L, Ning S, Chunmei L. Facile construction of porous intramolecular g-C_3N_4-based donor-acceptor conjugated copolymers as highly efficient photocatalysts for superior H_2 evolution. Nano Energy 2020;67:104273.
[24] Chunxue L, Huinan C, Chunbo L, Guangbo C, Paul AC, William ZX, Xiuyan W, Lihui L. Facile fabrication of g-C_3N_4 QDs/$BiVO_4$ Z-scheme heterojunction towards enhancing photodegradation activity under visible light. J Taiwan Inst Chem E 2019;95:669–81.
[25] Zhi L, Guangbo C, Wei J, Lihui L, Hairui W. Visible-light-driven CQDs@MIL-125(Ti) nanocomposite photocatalyst with enhanced photocatalytic activity for the degradation of etracycline. RSC Adv 2019;9:33238–45.
[26] Zhang M, Bai X, Liu D, Wang J, Zhu Y. Enhanced catalytic activity of potassium-doped graphitic carbon nitride induced by lower valence position. Appl Catal B Environ 2015;164:77–81.
[27] Ding J, Wang L, Liu Q, Chai Y, Liu X, Dai WL. Remarkable enhancement in visible-light absorption and electron transfer of carbon nitride nanosheets with 1% tungstate dopant. Appl Catal B Environ 2015;176–177:91–8.
[28] Tonda S, Kumar S, Kandula S, Shanker V. Fe-doped and-mediated graphitic carbon nitride nanosheets for enhanced photocatalytic performance under natural sunlight. J Mater Chem A 2014;2:6772–80.
[29] Hu SW, Yang LW, Tian Y, Wei XL, Ding JW, Zhong JX, Chu PK. Simultaneous nanostructure and heterojunction engineering of graphitic carbon nitride via in situ Ag doping for enhanced photoelectrochemical activity. Appl Catal B Environ 2015;163:611–22.
[30] Wang Y, Wang Y, Li Y, Shi H, Xu Y, Qin H, Li X, Zuo Y, Kang S, Cui L. Simple synthesis of Zr-doped graphitic carbon nitride towards enhanced photocatalytic performance under simulated solar light irradiation. Catal Commun 2015;72:24–8.
[31] Liu Q, Shen J, Yu X, Yang X, Liu W, Yang J, Tang H, Xu H, Li H, Li Y, Xu J. Unveiling the origin of boosted photocatalytic hydrogen evolution in simultaneously (S, P,

O)-codoped and exfoliated ultrathin g-C_3N_4 nanosheets. Appl Catal B 2019;248:84–94.
[32] Wei F, Liu Y, Zhao H, Ren X, Liu J, Hasan T, Chen L, Li Y, Su BL. Oxygen self-doped g-C_3N_4 with tunable electronic band structure for unprecedentedly enhanced photocatalytic performance. Nanocale 2017;00:1–3.
[33] Fu JW, Zhu BC, Jiang CJ, Cheng B, You W, Yu JG. Hierarchical porous O-doped g-C_3N_4 with enhanced photocatalytic CO_2 reduction activity. Small 2017;13:1603938.
[34] Zahrs S-G, Aliea N-E. As-synthesized ZSM-5 zeolite as a suitable support for increasing the photoactivity of semiconductors in a typical photodegradation process. Mater Sci Semicond Process 2015;39:265–75.
[35] Reddy GR, Balasubramanian S, Chennakesavulu K. Zeolite encapsulated active metal composites and their photocatalytic studies for rhodamine-B, reactive red-198 and chloro-phenols. RSC Adv 2015;5:81013–23.
[36] Guesh K, Álvaro M, M-Á Carlos, Chebude Y, Díaz I. Enhanced photocatalytic activity of TiO_2 supported on zeolites tested in real wastewaters from the textile industry of Ethiopia. Micropor Mesopor Mater 2016;225:88–97.
[37] Prakash K, Karuthapandian S, Senthilkumar S. Zeolite nanorods decorated g-C_3N_4 nanosheets: a novel platform for the photodegradation of hazardous water contaminants. Mater Chem Phys 2019;221:34–46.
[38] Khanh BV, Dai-Viet NV, Nhan THL, Tuan DL, Seong SH, Kwon TL. Co^{2+} substituted for Bi^{3+} in $BiVO_4$ and its enhanced photocatalytic activity under visible LED light irradiation. RSC Adv 2019;9:23526.
[39] Cao SW, Low JX, Yu JG, Jaroniec M. Polymeric photocatalysts based on graphitic carbon nitride. Adv Mater 2015;27:2150–76.
[40] Wang X, Maeda K, Thomas A, Takanabe K, Xin G, Carlsson JM, Domen K, Antonietti M. A metal-free polymeric photocatalyst for hydrogen production from water under visible light. Nat Mater 2009;8:76–80.
[41] Fang LJ, Wang XL, Zhao JJ, Li YH, Wang YL, Du XL, He ZF, Zeng HD, Yang H. One-step fabrication of porous oxygen-doped g-C_3N_4 with feeble nitrogen vacancies for enhanced photocatalytic performance. Chem Commun 2016;52:14408–11.
[42] Jesudoss SK, Vijaya JJ, Kaviyarasu K, Kennedy LJ, Ramalingam RJ, Al-Lohedan HA. Anti-cancer activity of hierarchical ZSM-5 zeolites synthesized from rice-based waste materials. RSC Adv 2018;8:481–90.
[43] Prakash K, Karuthapandian S, Senthilkumar S. Zeolite nanorods decorated g-C_3N_4 nanosheets: a novel platform for the photodegradation of hazardous water contaminants. Mater Chem Phys 2019;221:34–46.
[44] Zhu YP, Ren TZ, Yuan ZY. Mesoporous phosphorus-doped g-C_3N_4 nanostructured flowers with superior photocatalytic hydrogen evolution performance. ACS Appl Mater Interfaces 2015;7:16850–6.
[45] Sun Y, Zhang W, Xiong T, Zhao Z, Dong F, Wang R, Ho WK. Growth of BiOBr nanosheets on C_3N_4 nanosheets to construct two-dimensional nanojunctions with enhanced photoreactivity for NO removal. J Colloid Interface Sci 2014;418:317–23.
[46] Liang Q, Li Z, Yu X, Huang ZH, Kang F, Yang QH. Macroscopic 3D porous graphitic carbon nitride monolith for enhanced photocatalytic hydrogen evolution. Adv Mater 2015;27:4634–9.
[47] Huang HW, Xiao K, Tian N, Dong F, Zhang TR, Du X, Zhang YH. Template free precursor-surface-etching route to porous, thin g-C_3N_4 nanosheets for enhancing photocatalytic reduction and oxidation activity. J Mater Chem A 2017;5:17452–63.
[48] Kumar PS, Sobiya S, Selvakumar M, Babu SG, Karuthapandian S. Hierarchically structured CuO/g-C_3N_4 heterogeneous semiconductor photocatalyst with improved photocatalytic activity and stability. Energy Environ Focus 2016;5:1–11.
[49] Wei Z, Liu M, Zhang Z, Yao W, Tan H, Zhu Y. Efficient visible-light-driven selective oxygen reduction to hydrogen peroxide by oxygen-enriched graphitic carbon nitride polymers. Energy Environ Sci 2018;11:2581–9.
[50] Wang P, Shen B, Gao J. Synthesis of ZSM-5 zeolite from expanded perlite and its catalytic performance in FCC gasoline aromatization. Catal Today 2007;125:155–62.
[51] Zhang W, Wang K, Yu Y, He H. TiO_2/HZSM-5 nano-composite photocatalyst: HCl treatment of NaZSM-5 promotes photocatalytic degradation of methyl orange. Chem Eng J 2010;163:62–7.
[52] Wei F, Liu Y, Zhao H, Ren X, Liu J, Hasan T, Chen L, Li Y, Su B-L. Oxygen self-doped g-C_3N_4 with tunable electronic band structure for unprecedentedly enhanced photocatalytic performance. Nanoscale 2018;10:4515–22.
[53] Aanchal BS, Basu S. Complete removal of endocrine disrupting compound and toxic dye by visible light active porous g-C_3N_4/H-ZSM-5 nanocomposite. Chemosphere 2020;241:124981.
[54] Li J, Shen B, Hong Z, Lin B, Gao B, Chen Y. A facile approach to synthesize novel oxygen-doped g-C_3N_4 with superior visible-light photo reactivity. Chem Commun 2012;48:12017–9.
[55] Samanta S, Yadav R, Kumar A, Sinha AK, Srivastava R. Surface modified C, O co-doped polymeric g-C_3N_4 as an efficient photocatalyst for visible light assisted CO_2 reduction and H_2O_2 production. Appl Catal B 2019;259:118054.
[56] Zhao GX, Liu GG, Pang H, Liu HM, Zhang HB, Chang K, Meng XG, Wang XJ, Ye J. Improved photocatalytic H_2 evolution over g-carbon nitride with enhanced in-plane ordering. Small 2016;12:6160–6.
[57] Shi L, Yang L, Zhou W, Liu Y, Yin L, Hai X, Song H, Ye J. Photo assisted construction of holey defective g-C_3N_4 photocatalysts for efficient visible-light-driven H_2O_2 production. Small 2018;14(9):1703142.
[58] Jiang Y, Liu P, Chen YC, Zhou Z, Yang H, Hong Y, Li F, Ni L, Yan Y, Gregory DH. Construction of stable Ta_3N_5/g-C_3N_4 metal/non-metal nitride hybrids with enhanced visible-light photocatalysis. Appl Surf Sci 2017;391:392–403.
[59] You Z, Su Y, Yu Y, Wang H, Qin T, Zhang F, Shen Q, Yang H. Preparation of g-C_3N_4 nanorod/$InVO_4$ hollow sphere composite with enhanced visible-light photocatalytic activities. Appl Catal B 2017;213:127–35.
[60] Zhang Z, Liu K, Feng Z, Bao Y, Dong B. Hierarchical sheet-on-sheet $ZnIn_2S_4$/g-C_3N_4 heterostructure with highly efficient photocatalytic H_2 production based on photoinduced interfacial charge transfer. Sci Rep 2016;6:1–10.
[61] Li Z, Jin C, Wang M, Kang J, Wu Z, Yang D, Zhu T. Novel rugby-like g-C_3N_4/$BiVO_4$ core/shell Z-scheme composites prepared via low-temperature hydrothermal method for enhanced photocatalytic performance. Sep Purif Technol 2020;232:115937.
[62] Ahmed S, Rasul MG, Martens WN, Brown R, Hashib MA. Heterogeneous photocatalytic degradation of phenols in wastewater: a review on current status and developments. Desalination 2010;261(1–2):3–18.
[63] Chen F, Yang Q, Li X, Zeng G, Wang D, Niu C, Zhao J, An H, Xie T, Deng Y. Hierarchical assembly of graphene-bridged Ag_3PO_4/Ag/$BiVO_4$ (040) Z-scheme photocatalyst: an efficient, sustainable and heterogeneous catalyst with enhanced visible-light photoactivity towards tetracycline degradation under visible light irradiation. Appl Catal B 2017;200:330–42.
[64] Chen F, Yang Q, Zhong Y, An H, Zhao J, Xie T, Xu Q, Li X, Wang D, Zeng G. Photoreduction of bromate in drinking water by metallic Ag and reduced graphene oxide (RGO) jointly modified $BiVO_4$ under visible light irradiation. Water Res 2016;101:555–63.
[65] Bifu L, Min C, Zhengyuan Z, Jie X, Di L, Dongbo X, Weidong S. Highly efficient visible-light-driven photocatalytic degradation of tetracycline by a Z Scheme g-C_3N_4/Bi_3TaO_7 nanocomposite photocatalyst. Dalton Trans 2017;46:8431–8.
[66] Prakash K, Karuthapandian S, Senthilkumar S. Zeolite nanorods decorated g-C_3N_4 nanosheets: a novel platform for the photodegradation of hazardous water contaminants. Mater Chem Phys 2019;221:34–46.
[67] Jingjing Y, Hongqing Z, Yuan P, Pengxi L, Shuyan C, Bing Y, Jinzhong Z. Photocatalytic performance and degradation pathway of Rhodamine B with TS-1/C_3N_4 composite under visible light. Nanomaterials 2020;10:756.
[68] Hao W, Yaoxing H. One step synthesis of efficient photocatalysts by TCAP doped g-C_3N_4 for enhanced visible-light photocatalytic activity. New J Chem 2020;44:1127–37.